Die Grenzen der Chemie neu ausloten? It takes #HumanChemistry

Wir suchen kreative Chemikerinnen und Chemiker, die mit uns gemeinsam neue Wege gehen wollen – mit Fachwissen, Unternehmertum und Kreativität für innovative Lösungen. Informieren Sie sich unter:

evonik.de/karriere

EVONIK
Leading Beyond Chemistry

ADVANCED FUNCTIONAL MATERIALS
www.afm-journal.de

Morphology Transformation Pathway of Block Copolymer-Directed Cooperative Self-Assembly of ZnO Hybrid Films Monitored In Situ during Slot-Die Coating

*Ting Tian, Shanshan Yin, Suo Tu, Christian L. Weindl, Kerstin S. Wienhold, Suzhe Liang, Matthias Schwartzkopf, Stephan V. Roth, and Peter Müller-Buschbaum**

Cooperative self-assembly (co-assembly) of diblock copolymers (DBCs) and inorganic precursors that takes inspiration from the rich phase separation behavior of DBCs can enable the realization of a broad spectrum of functional nanostructures with the desired sizes. In a DBC assisted sol–gel chemistry approach with polystyrene-*block*-poly(ethylene oxide) and ZnO, hybrid films are formed with slot-die coating. Pure DBC films are printed as control. In situ grazing-incidence small-angle X-ray scattering measurements are performed to investigate the self-assembly and co-assembly process during the film formation. Combining complementary ex situ characterizations, several distinct regimes are differentiated to describe the morphological transformations from the initially solvent-dispersed to the ultimately solidified films. The comparison of the assembly pathway evidences that the key step in the establishment of the pure DBC film is the coalescence of spherical micelles toward cylindrical domains. Due to the presence of the phase-selective precursor, the formation of cylindrical aggregates in the solution is crucial for the structural development of the hybrid film. The pre-existing cylinders in the ink impede the domain growth of the hybrid film during the subsequent drying process. The precursor reduces the degree of order, prevents crystallization of the PEO block, and introduces additional length scales in the hybrid films.

1. Introduction

Mesoporous ZnO thin films have sparked tremendous attention due to their morphological richness and advantageous functionalities,[1,2] which promise enormous perspectives in important fields including photocatalysis,[3,4] gas sensing,[5–7] biomedical science,[8,9] energy storage, and conversion.[10,11] Among the different existing synthetic routes for ZnO, the self-assembly of amphiphilic diblock copolymers (DBCs) has emerged as a very versatile and powerful strategy because of its incomparable merits in both highly tunable morphology and superior fabrication flexibility.[12] Inspired by their rich phase separation behaviors as well as the well-established theoretical phase diagrams, this soft-templating approach has been extensively documented to access a multitude of functionalized metal oxides or inorganic nanoparticles with desirable morphology and orientation besides ZnO.[13,14] However, the successful realization of ZnO nanostructures guided by self-assembled DBCs involves tedious fabrication procedures and requires a delicate control over the entire process with a high sensitivity to humidity and temperature.[15,16] In particular, up-scaling can be challenging. Therefore, a well-reproducible and easily up-scalable protocol for the fabrication of mesoporous ZnO coatings is still absent today.

Conceptually, a successful fabrication of ZnO nanostructures templated by DBCs acutely depends on the cooperative self-assembly (co-assembly) of amphiphilic DBC molecules and inorganic sol–gel precursor molecules.[17,18] During self-assembly

T. Tian, S. Yin, S. Tu, C. L. Weindl, K. S. Wienhold, S. Liang, P. Müller-Buschbaum
Lehrstuhl für Funktionelle Materialien
Physik-Department
Technische Universität München
James-Franck-Str. 1, 85748 Garching, Germany
E-mail: muellerb@ph.tum.de

The ORCID identification number(s) for the author(s) of this article can be found under https://doi.org/10.1002/adfm.202105644.

DOI: 10.1002/adfm.202105644

M. Schwartzkopf, S. V. Roth
Deutsches Elektronen-Synchrotron DESY
Notkestr. 85, 22603 Hamburg, Germany

S. V. Roth
Department of Fiber and Polymer Technology
KTH Royal Institute of Technology
Teknikringen 56-58, Stockholm SE-100 44, Sweden

P. Müller-Buschbaum
Heinz Maier-Leibnitz Zentrum (MLZ)
Technische Universität München
Lichtenbergstr. 1, 85748 Garching, Germany

processes occurring in the initial solution used for coating and the coating after deposition, the ZnO nanostructure is formed. It is driven by interfacial interactions originating from the preferential incorporation of the precursor guest molecules into the corona chains of the polymer host matrix, mostly through hydrogen bonding. This complex interplay makes the hybrid systems more complicated than the bare DBC systems.[19] Apart from the components themselves, the solvent affinity, precursor cross-linking, solvent evaporation rate, and substrate wettability also have a straightforward impact on the interfacial area and polymer chain stretching.[20,21] Such complexity often leads to the formation of kinetically frozen nanostructures, deviating from the equilibrium state. Consequently, an additional post-treatment step (mainly through solvent vapor or thermal annealing) is always essential to impart sufficient mobility to the polymer chains, yielding a further structural arrangement, and ultimately achieving high periodicity of the nanostructure.[22,23]

Benefiting from the good solution processability, this wet-chemical approach is capable of being integrated into industrial-based production processes such as sheet-to-sheet and roll-to-roll (R2R) techniques, which offer the opportunities for cost-effectively achieving high-throughput manufacturing of large-area coatings. Among these large-scale fabrication routes, slot-die coating possesses considerable potential for applications such as organic electronics and photovoltaics in terms of controllable film morphologies and achievable device performance.[24–26] In contrast to the kinetically trapped morphologies generated from the widespread use of spin coating, slot-die coating, a non-contact meniscus-guided printing method, allows for fine-tuning of the film deposition process. The coating can be tuned by virtue of optimization of deposition parameters, including the ink viscosity, the slot-die head geometry, and the fluid flow conditions.[27,28] Concerning the underlying film formation mechanism, in situ grazing-incidence small-angle X-ray scattering (GISAXS) demonstrated to be a powerful tool for real-time monitoring of the solvent-evaporation-induced morphology evolution at the nanometer scale. Besides, both film surface and buried nanostructures are detectable. Thus, morphological features with high statistical significance can be resolved by this reciprocal-space technique.[29] For example, on the basis of in situ GISAXS measurements, Pröller et al. and Liu et al. successfully mapped the multistage structure forming process of photoactive layers during slot-die coating.[30,31] Berezkin et al. and Gu et al. followed morphological transformations of DBC films under solvent vapor annealing conditions.[32,33] Sarkar et al. and Song et al. disclosed the time-resolved kinetics of spray coating of inorganic ZnO films and titania films, respectively.[34,35] Moreover, with an ultrahigh time resolution at the subsecond level, GISAXS also enables the detection of short-lived intermediate phases that occurred in rapid DBCs ordering dynamics: Fleury et al. and Franeker et al. observed multiple transient structures and elucidated the phase separation during spin coating.[36,37] In situ studies of thin-film coating processes have been reported, but only a very limited number of studies have been carried out yet to follow the fabrication of organic–inorganic hybrid film using in situ GISAXS during slot-die coating. Also, the mesoporous structures synthesized by applying DBCs as pore-forming agents, so far have been primarily investigated post-fabrication of the ZnO coatings. In addition, implementing ZnO/polymer hybrids as cathode buffer layers has emerged as a promising and effective approach to achieve polymer-based solar cells with high performance. By virtue of the synthetic effects of the insulating polymer and inorganic ZnO nanoparticles, the ZnO/polymer hybrids provide a simple way to manipulate electron transport. In this perspective, the structure control of resultant ZnO/polymer hybrids is also of crucial significance for further device optimization.[38,39] However, to gain more fundamental understanding, a real-time characterization of the complex self-assembly behaviors occurring during the conversion of the fluid solution toward the solidified film in the sol–gel process during printing is of vital importance.

Hence, herein in situ GISAXS experiments are conducted to access the morphology evolution during the solution-to-film transition accomplished through slot-die coating. The co-assembly in the hybrid system in conjunction with self-assembly in the pure polymer system is systematically characterized to explore the structure-guiding effect of the DBC for the formation of the ZnO architectures. In the present work, the templated ZnO films are deposited from a micellar solution consisting of the commonly used DBC polystyrene-*block*-poly(ethylene oxide) (PS-*b*-PEO) and a so-called good–poor solvent pair, one common for both blocks PS and PEO, and one selective toward only PEO. Following an identical recipe, the establishment of the PS-*b*-PEO/ZnO hybrid film is accomplished through the introduction of ZnO precursor molecules. Additionally, the solvent selectivity-derived nanophase separation in solution is verified using dynamic light scattering (DLS) and complementary small-angle X-ray scattering (SAXS) measurements. Ex situ morphological observations of the completely dried film are carried out via scanning electron microscopy (SEM) and GISAXS. Thus, we are able to track the structural development from the initial solutions to the ultimate films after printing. During printing, the slot-die head is kept fixed while moving the stage with the substrate as common in R2R coating. With in situ GISAXS, several distinct regimes during the film formation are identified, and the underlying morphology forming mechanism leading to final phase-separated nanostructures is elucidated. All together, we visualize the ZnO nanostructure formation during the slot-die coating process. This sheds light on a well-controllable tailoring of the mesoporous morphology templated by DBCs toward a broad spectrum of technological applications of the ZnO coatings.

2. Result and Discussion

2.1. Preassembly in Solution

The amphiphilic DBC investigated in the present work has an average molecular weight of 20.5 and 8.0 kg mol^{-1} for hydrophobic PS and hydrophilic PEO blocks, respectively. Thus, the volume fraction of the PEO segments is $f_{PEO} = 0.27$ according to the corresponding bulk densities.[40] To trigger the microphase separation in solution, the cosolvent used is binary *N*,*N*′-dimethylformamide–water (DMF–H_2O) mixtures, in which DMF is a good solvent for both PS and PEO blocks, while H_2O is selective toward PEO in light of the Hansen solubility parameters.[41] Consequently, the formation of crew-cut micelles is typically characterized by a two-step organization process, where DMF promotes an equivalent level of chain stretching for both blocks,

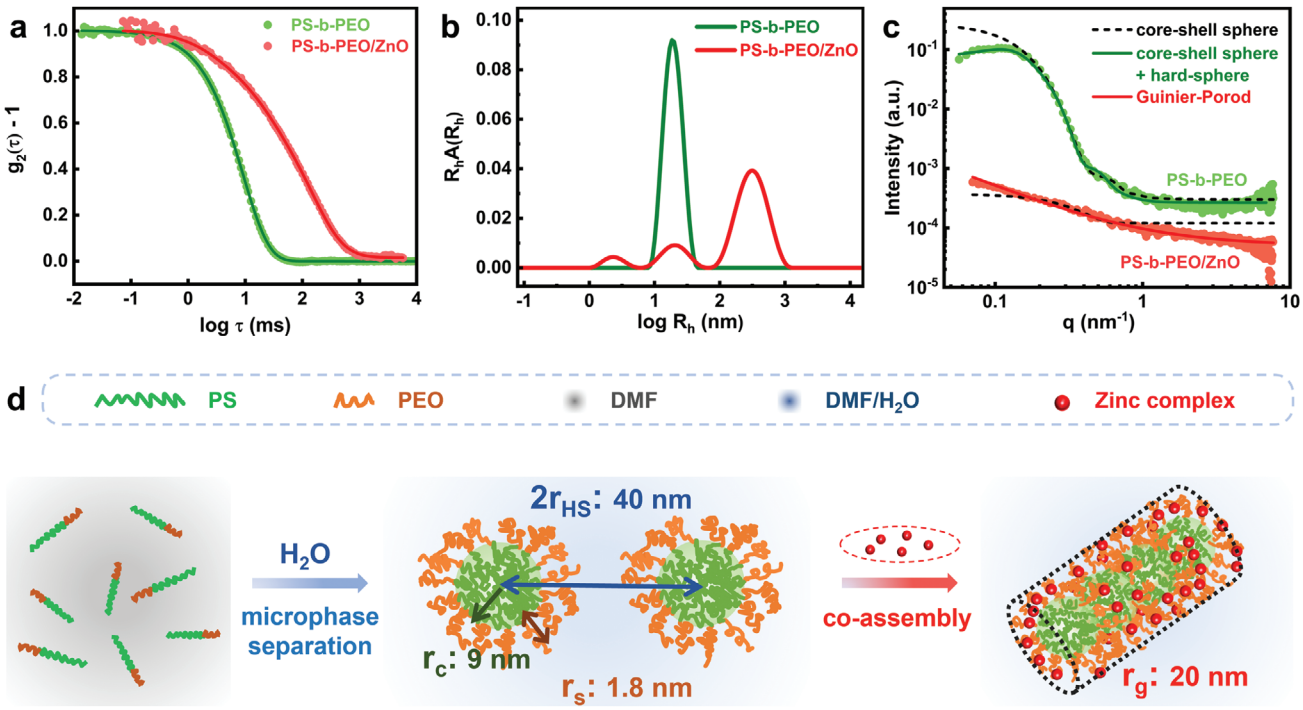

Figure 1. Structural information of PS-*b*-PEO and PS-*b*-PEO/ZnO in solution. a) DLS normalized autocorrelation function profiles. The solid lines indicate the best fit results to the measured data (symbols). b) Corresponding distribution functions of hydrodynamic radii, R_h, acquired from the lag time curves. c) SAXS scattering curves (symbols) and the model fits (lines). d) Schematic of the spherical-to-cylindrical morphological transformation of the PS-*b*-PEO micelles induced by selectively localized ZnO precursor.

while the affinity of H_2O toward PEO enhances the incompatibility between them. This incompatibility stimulates the spontaneous phase separation into spherical micelles consisting of a less hydrated PS core and a highly swollen PEO corona. These self-assembled micelles serve as nano-templates after the introduction of the inorganic precursor molecules. It is assumed that the hydrolyzed Zn^{2+} species are selectively distributed in the PEO moieties via hydrogen bonding, which significantly influences the interfacial behavior and might yield different morphologies.

DLS measurements enable the analysis of the micellization and possible aggregation by determining the overall dimensions in terms of hydrodynamic radius (R_h). **Figure 1**a presents the representative normalized intensity autocorrelation functions measured for the DBC solution with and without precursor zinc acetate dihydrate (ZAD).

The PS-*b*-PEO solution features a single decay, suggesting that a single category of diffusing particles prevails and is tentatively assigned to micelles. After the incorporation of ZAD, the decay curve displays a pronounced shift toward larger lag time (τ), which is presumably attributed to the formation of large-sized aggregates. The corresponding distribution functions extracted from the related fits are shown in Figure 1b. The PS-*b*-PEO solution shows a narrow size distribution with a unimodal peak centered at 20 ± 2 nm, whereas the ZnO-loaded PS-*b*-PEO (PS-*b*-PEO/ZnO) solution displays a trimodal broad radius distribution including an identical peak related to PS-*b*-PEO micelles. Given the irreversible fusion of PS-*b*-PEO micelles carrying the Zn—O covalent bonds,[18] the much larger R_h located at 343 ± 15 nm has a high amplitude, corresponding to formed intermicellar aggregates. In addition, the R_h with sizes below 10 nm might arise from the clustering of ZAD molecules or molecularly dissolved polymer chains. As for the further structural assignment of the smallest R_h, additional DLS measurements of both, pure polymer and precursor solutions are performed. In the pure solution without any water addition (Figure S2, Supporting Information), the peak associated with the fast decay in the measured autocorrelation function is centered at 3.6 nm, which is comparable to that of the hybrid film. Such evidence supports the presence of molecularly dissolved PS-*b*-PEO polymer chains in the hybrid solution. Only providing overall information on the R_h, DLS analysis is, unfortunately, incapable of determining the structural origin of the different size distribution and the dramatically increased R_h in the hybrid PS-*b*-PEO/ZnO solution. One explanation could be the transformation into cylindrical structures,[42] since such a spherical-to-cylindrical morphology transition was reported for DBC micelle-templating systems.[43,44]

Therefore, SAXS experiments are conducted in a complementary manner to extract more precise information about the micelle solution, in particular, the micellar shape and internal micelle structure. The corresponding SAXS profiles are depicted in Figure 1c. Despite an analogous scattering behavior in both, intermediate-q and high-q regions, the SAXS data of both solutions are different. The scattering curve of the PS-*b*-PEO solution exhibits a visible shoulder in the low-q region, while the PS-*b*-PEO/ZnO solution features nearly straight line-shaped intensity decay in the low-q region. As for the model-dependent data analysis, the initial approximation following a simple core–shell sphere model fails to fit the overall q range for both systems. In the case of the PS-*b*-PEO solution, only

part of the low-q region cannot be explained, suggesting that the scattering contribution from the spatial correlation between the micelles is not negligible.[45] To account for this, an additional hard-sphere structure factor is used to explain the low-q region. Such a modified model based on the combination of core–shell sphere form factor and hard-sphere structure factor, turns out to enable a successful fit for the PS-*b*-PEO micelles in solution. As summarized (see Table S3, Supporting Information), the spherical core–shell micelle has a radius (r_{mic}) of 10.8 ± 0.3 nm, in which the PS core radius (r_c) is 9.0 ± 0.1 nm and PEO shell thickness (r_s) is 1.8 ± 0.2 nm. Such a much shorter corona-forming block is expected for crew-cut micelles. The hard-sphere radius (r_{HS}) and the volume fraction (ν_{HS}) of the correlated PS-*b*-PEO micelles are 20 ± 1 nm and 0.10 ± 0.01, respectively. Such weak intermicellar interactions might originate from the semi-dilute concentration and increase the tendency to aggregation.[46,47] Matching only for a very narrow q range, the core–shell sphere model is invalid for fitting the SAXS data of the PS-*b*-PEO/ZnO solution. Thus, we can exclude the possibility of a simple shell expansion of the core–shell micelles after the accommodation of ZnO precursor molecules. Considering the observed aggregation in the DLS measurements, a Guinier–Porod model approach is adopted as an alternative and gives a satisfactory fit result over the entire q range.[48,49] This best model fit is established on several key structural parameters consisting of the radius of gyration (r_g), a shape factor (s), and Porod exponent (m).[50,51] The determined values are 20.0 ± 1.2 nm, 0.83 ± 0.01 and 1.00 ± 0.02, respectively. Consequently, a rigidly rod-like shape can be applied to describe the generated PS-*b*-PEO aggregates, and the length is calculated to be ≈15.5 nm. A more detailed model description and the extracted fit parameters can be found in Section S3, Supporting Information.

The presence of ZnO precursor leads to a spherical-to-cylindrical morphology transition, implying the occurrence of a 1D directional coalescence process of the ZnO-loaded PS-*b*-PEO micelles as a result of interfacial energy minimization (Figure 1d). Such information is of special importance as the co-assembly of the ZnO-loaded micelles in solution is a sophisticated process, wherein the hydrolyzed and condensed products of ZnO precursors would give rise to permanent Zn—O covalent bonds with adjacent ZnO species on PEO moieties, and the formation of such an interconnected network is irreversible.[18]

2.2. Assembled Morphology in Thin Film Geometry

The formation of micelles/aggregates as mentioned above can be considered as a consequence of the preassembly in solution. Despite having completely different structures in the solution states (ink for the printing), both films demonstrate similar overall morphologies after printing. According to self-consistent field theory,[52] a dispersion of the minor PEO cylinders in the PS matrix is expected in the film geometry. As displayed in **Figure 2**a, a typical fingerprint-like morphology for the slot-die-coated PS-*b*-PEO film surface can be observed, in which darker PEO domains alternate to a brighter PS matrix. Highlighted by the red circle and blue rectangle in Figure 2a, respectively, the round and elongated dark PEO domains coexist. From the corresponding 45° tilt-view image (Figure S4a, Supporting Information), the PS-*b*-PEO film is found to be very thin with some short PEO cylinders perpendicularly oriented to the Si substrate. Returning to the film surface, the round PEO domains are identified to be vertically aligned, while the elongated ones might be parallel cylinders or coalesced vertical PEO domains. Similar morphology has been observed for the PS-*b*-PEO film.[53] Additionally, the ring present in the 2D fast Fourier transform (2D-FFT) pattern reveals a short-range order for the slot-die-coated PS-*b*-PEO film. From the corresponding power spectral density (PSD) profile extracted from the 2D-FFT pattern (Figure S5, Supporting Information), the periodic interdomain spacing on the film surface can be derived to be 27 nm according to Bragg's law $d = 2\pi/q$. Compared to kinetically trapped granular morphologies observed in the spin-coated counterpart films (Figure S6a, Supporting Information), the well-ordered nanostructures achieved by slot-die coating can be attributed to a slower solvent evaporation rate, which ensures sufficient time as well as chains mobility to enable further structural developments.[54] In addition, such a morphology difference can be interpreted from the viewpoint of the film formation mechanism. Unlike spin coating, in which the centrifugal force controls the film formation process and non-equilibrium morphologies are easily frozen-in, slot-die coating is a kind of meniscus-guided technique involving more complicated fluid flow and gradients in combination with sufficient chain mobility, which is advantageous for improving phase separation and structural order.[55]

After the incorporation of the ZnO component, the SEM image of the PS-*b*-PEO/ZnO hybrid film shows significantly enhanced contrast owing to the highly conductive nature of ZnO (Figure 2a and Figure S4b, Supporting Information). The preferential segregation of brighter ZnO objects inside both round (marked by the red circle in the upper image in Figure 2a) and elongated (marked by the blue rectangle in the upper image in Figure 2a) PEO regions is visible, separating the hybrid film into ZnO-incorporated PEO domains (denoted as PEO/ZnO) and PS domains. Indeed, a well-retained morphology is also easily discernible, evidencing the structure-directing effect from the polymer template to a large degree. Unfortunately, the structure order of PS-*b*-PEO film is destroyed by the selective localization of ZnO as confirmed from the absence of an FFT ring, which is often the case for DBC films with an incorporated third component.[56] The possible scenario for this loss in order originates from the loss of the conformational entropy of the polymer chains by the ZnO accommodation.[57] Different from the morphology of the slot-die-coated hybrid film, but similar to the spin-coated pure DBC film, the spin-coated hybrid film also shows pronounced selective confinement of ZnO inside the PEO domains (Figure S6b, Supporting Information).

To access the inner morphologies, particularly to quantify the structure sizes and spatial correlations of a selected component, GISAXS measurements are performed at an incident angle above the critical angles of all involved materials.[29] As highlighted by a solid yellow arrow (Figure 2b), the presence of a prominent rod-like Bragg reflection in the PS-*b*-PEO film data, again signifies the ordered arrangement of the as-obtained PS-*b*-PEO nanostructures. Based on the calculation of the scattering length density, the material-specific Yoneda

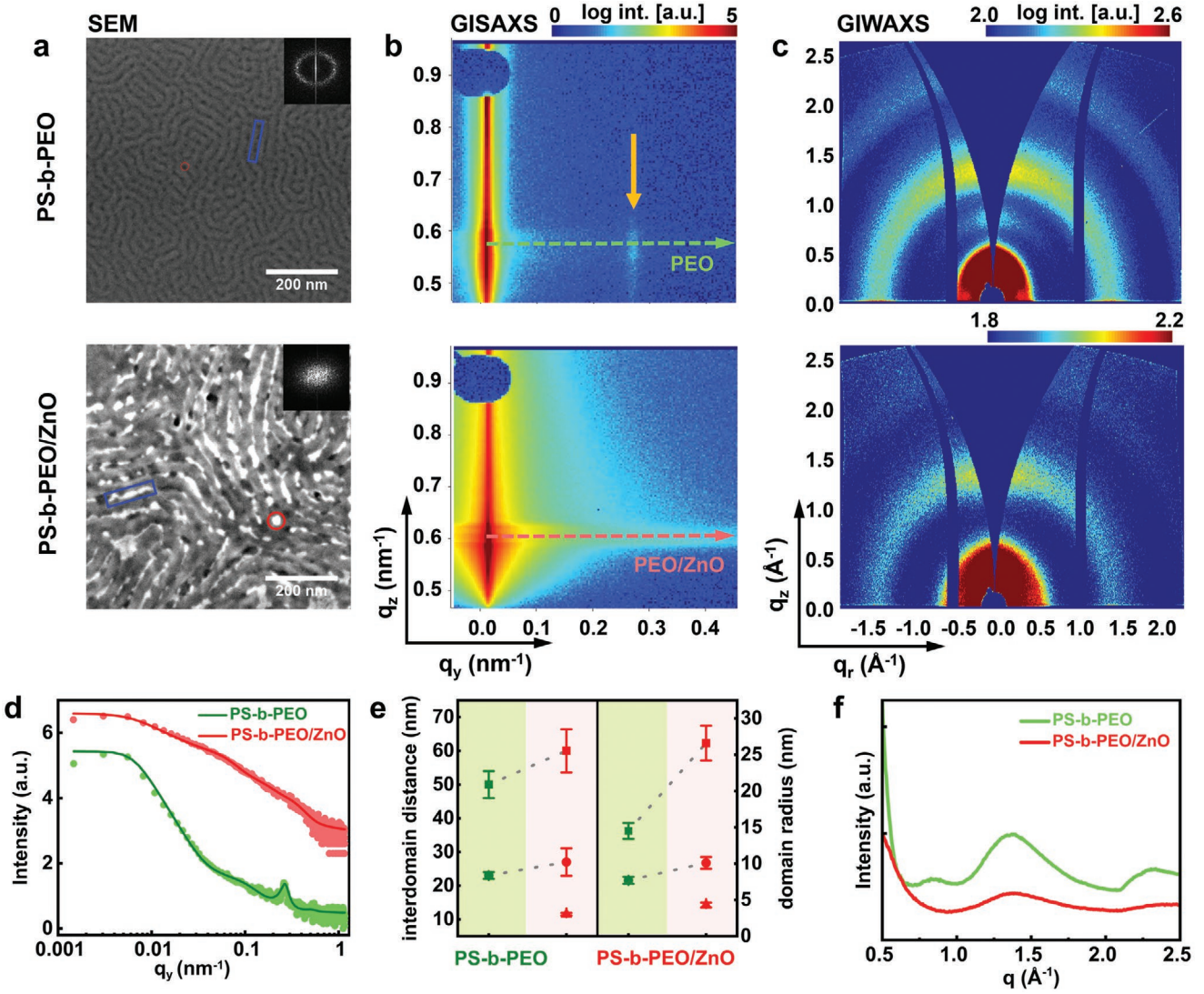

Figure 2. a) High-magnification (80 k) SEM top-view images of completely solidified PS-*b*-PEO (top) and PS-*b*-PEO/ZnO hybrid film (bottom) after slot-die coating. The blue rectangles and red circles highlight worm-like and sphere-shaped PEO domains (PEO/ZnO domains in the PS-*b*-PEO/ZnO film), respectively. The upper-right insets are the corresponding 2D FFT patterns. b) 2D GISAXS data. The dashed green arrow and the dashed red arrow along q_y direction schematically display the Yoneda peak positions of PEO and PEO/ZnO domains for performing horizontal line cuts, respectively. The yellow arrow in pure PS-*b*-PEO film data indicates the appearance of the characteristic peak related to the domain spacing. c) 2D GIWAXS data. d) Horizontal line cuts (solid dots) from GISAXS data with best fits (solid lines). e) Characteristic interdomain distance and domain size of small-sized (triangles), middle-sized (spheres), and large-sized structures (squares), respectively. The dashed lines are guides to the eyes. f) Radial cake cuts from the 2D GIWAXS data providing pseudo-XRD information.

peak of PEO is determined to be at $q_z = 0.5712$ nm^{-1} (pointed out as dashed green arrow). Interestingly, the introduction of the high-electron-density ZnO phase not only causes a much stronger lateral scattering observed from the PS-*b*-PEO/ZnO hybrid film, but also alters the propagation of the scattering signals along the q_z direction, leading to multiple intensity modulations and a distinguishable splitting of the Yoneda region due to the X-ray interference effect (Figure 2b).[58,59] Among these triple Yoneda peaks, the one for PEO/ZnO domains can be observed at $q_z = 0.6291$ nm^{-1} as indicated by the dashed red arrow. More detailed analysis of these intensity oscillations and the assignment of the Yoneda peak of PEO/ZnO domains can be found in Section S6, Supporting Information. The pronounced Bragg peak seen in the case of the pure DBC film vanishes for the hybrid film, which is in line with the lack of structural order observed on the film surface with SEM. To track the structural changes by ZnO embedment in more detail, the intensity line cuts along the horizontal direction (q_y) are taken at the q_z positions of the critical angles of respective domains (PEO domains for PS-*b*-PEO film and PEO/ZnO domains for PS-*b*-PEO/ZnO film). As plotted in Figure 2d, the observed Bragg peak is again found to be located at $q_y = 0.26$ nm^{-1}, which closely matches the characteristic peak in PSD for the PS-*b*-PEO film, confirming that the characteristic spatial periodicity not only occurs on the film surface but spans the entire film thickness. From a fit, the corresponding full-width at half maximum

(FWHM) of the peak is quantified to be 0.0683 ± 0.0004 nm^{-1}. Thereby the correlation length (over which the structural order of the cylindrical structures persist) can be estimated to be 83 nm according to the Scherrer analysis,[51,54,60] indicating that this polymer film possesses only short-range order in good agreement with the absence of higher-order Bragg peaks. Also, the absence of the characteristic scattering from the hexagonally close-packed cylinders suggests that long-range order is not achieved in the printed DBC. In good accordance with the PSD profile in Figure S5, Supporting Information, the in-plane scattering curve for PS-*b*-PEO/ZnO film exhibits a plateau-like feature without any characteristic peak, which is indicative of the spatial disorder of the PEO/ZnO domains. For GISAXS data modeling, distorted-wave Born approximation is used to account for the multiple reflection/refraction effects, while the spatial distribution of the scattering entities is assumed in the framework of local monodisperse approximation. More data modeling details are described in Section S7, Supporting Information. Two differently sized objects are needed to fit the horizontal line cut of the PS-*b*-PEO data, whereas three are necessary for the PS-*b*-PEO/ZnO hybrid film. For each object, the form factor denotes the radius of the domains, while the respective structure factor correlates to the center-to-center distance between the adjacent domains. As plotted in Figure 2e, the two interdomain distances increase from 50 ± 4 and 23 ± 1 nm for PEO in the DBC film to 60 ± 6 and 27 ± 4 nm for PEO/ZnO in the hybrid film. Following a consistent tendency, the domain radii grow from 14.5 ± 1.1 and 7.7 ± 0.5 nm for PEO in the DBC film to 27 ± 2 and 10.1 ± 0.8 nm for PEO/ZnO in the hybrid film. Such an expansion of the interdomain spacing is a direct outcome of the swelling of PEO domains upon the preferential localization of ZnO. Besides, in the hybrid film appears a third type of object with an interdomain distance of 11.5 ± 0.4 nm and domain size of 4.2 ± 0.3 nm. Analogous phenomena concerning the deformation of structural order and the enlargement of the polymeric domains upon the integration of phase-selective molecules or particles were also found in previous investigations.[56,61] The detailed origin of the structural changes is tracked with in situ investigations as described below.

Considering that the melting temperature of PEO is well below the glass transition temperature of PS under the current experimental conditions, the PEO blocks could be crystalline, while PS would remain amorphous after the film formation processes.[40,46] Accordingly, ex situ grazing-incidence wide-angle X-ray scattering (GIWAXS) characterizations are performed to investigate the crystallization behavior of PS-*b*-PEO polymer upon the selective incorporation of the ZnO phase. As shown in the 2D GIWAXS data presented in Figure 2c, the characteristic crystallinity peaks of the PEO domain can be observed in the pure PS-*b*-PEO film, while the tethering of the ZnO phase to the PEO blocks appear to frustrate the crystallization, since amorphous diffraction features appear. The azimuthal integration of the 2D GIWAXS data provides pseudo X-ray diffraction (pseudo-XRD) data, which also corroborates the crystallinity loss of the PEO domains after ZnO is embedded (see Figure 2f). Accordingly, the strongest peaks in a q range of 1.0–2.0 $Å^{-1}$ can be attributed to diffraction from (120), (112), (222), and (111) planes, and another broad one at 2.0–2.5 $Å^{-1}$ is closely associated to (313) and (118) planes of PEO crystallites. In addition, another weak peak appears at around 0.80 $Å^{-1}$, which was previously found in crystalline PEO, but no definitive indexing was reported.[47,48] Therefore, the distribution of phase-selective ZnO yields the transition from crystalline to amorphous PEO domains. Similar phenomena were extensively witnessed in previous investigations, which suggested that the spatial distribution of PEO-selective components would reduce the chain length of crystallizable PEO and then inhibited the PEO crystallization due to the hydrogen-bonding interactions.[49]

2.3. Structural Transformation during Film Formation

Based on these initial observations, questions arise about the self-assembly pathways from spherical PS-*b*-PEO micelles toward cylindrical nanostructures in the film during the slot-die coating process. In addition, it is unknown how the co-assembly of the polymer template and ZnO precursors dictates their spatial distribution and determines the resultant morphology for the PS-*b*-PEO/ZnO hybrid film. To resolve possible intermediate structures and obtain detailed structural parameters about the film formation, time-resolved in situ GISAXS measurements are implemented during the printing in a R2R compatible mode, meaning that the slot-die head is kept fixed and the stage with the substrate is moving underneath. Considering that the water vapor in the atmosphere would interact with hydrophilic PEO or PEO/ZnO domains and give rise to possible morphology changes, especially under high humidity conditions,[62] both pure polymer and hybrid films in this work are slot-die-coated under identical ambient conditions (typically 23% relative humidity) to minimize the effects from a high relative humidity.

2.3.1. Slot-Die Coating of Pure Polystyrene-block-Poly(Ethylene Oxide) Film

The sketch of the in situ GISAXS setup is shown in **Figure 3**a. Figure 3b pictures the lateral structure evolution of PEO domains in the pure DBC film in a mapping extracted from horizontal line cuts of the in situ 2D GISAXS data. Selected 2D GISAXS data are displayed in Figure S9, Supporting Information. A rapidly evolving morphology is visible as evidenced from both, the scattering intensity increase and the appearance of the characteristic Bragg peak along the out-of-plane direction (dashed box in Figure 3b). The initial scattering intensity is low. Until t = 25 s, it increases strongly, followed by a weaker increase until reaching equilibrium. At t = 38 s, the pronounced Bragg reflection appears at around q_y = 0.26 nm^{-1}, indicating that the coronas of sphere-shaped PS-*b*-PEO micelles have been packed into ordered PEO cylinders. Note that from $t \geq 230$ s, neither scattering intensity nor Bragg peak changes can be observed, suggesting that the establishment of a morphologically stable PS-*b*-PEO film is accomplished. Figure 3d shows selected horizontal line cuts together with model fits as a function of time. No discernible scattering peak can be observed at the very beginning, which is indicative of the disordered state for the as-obtained wet film. As solvent leaves the film, the disorder-to-order transition occurs and

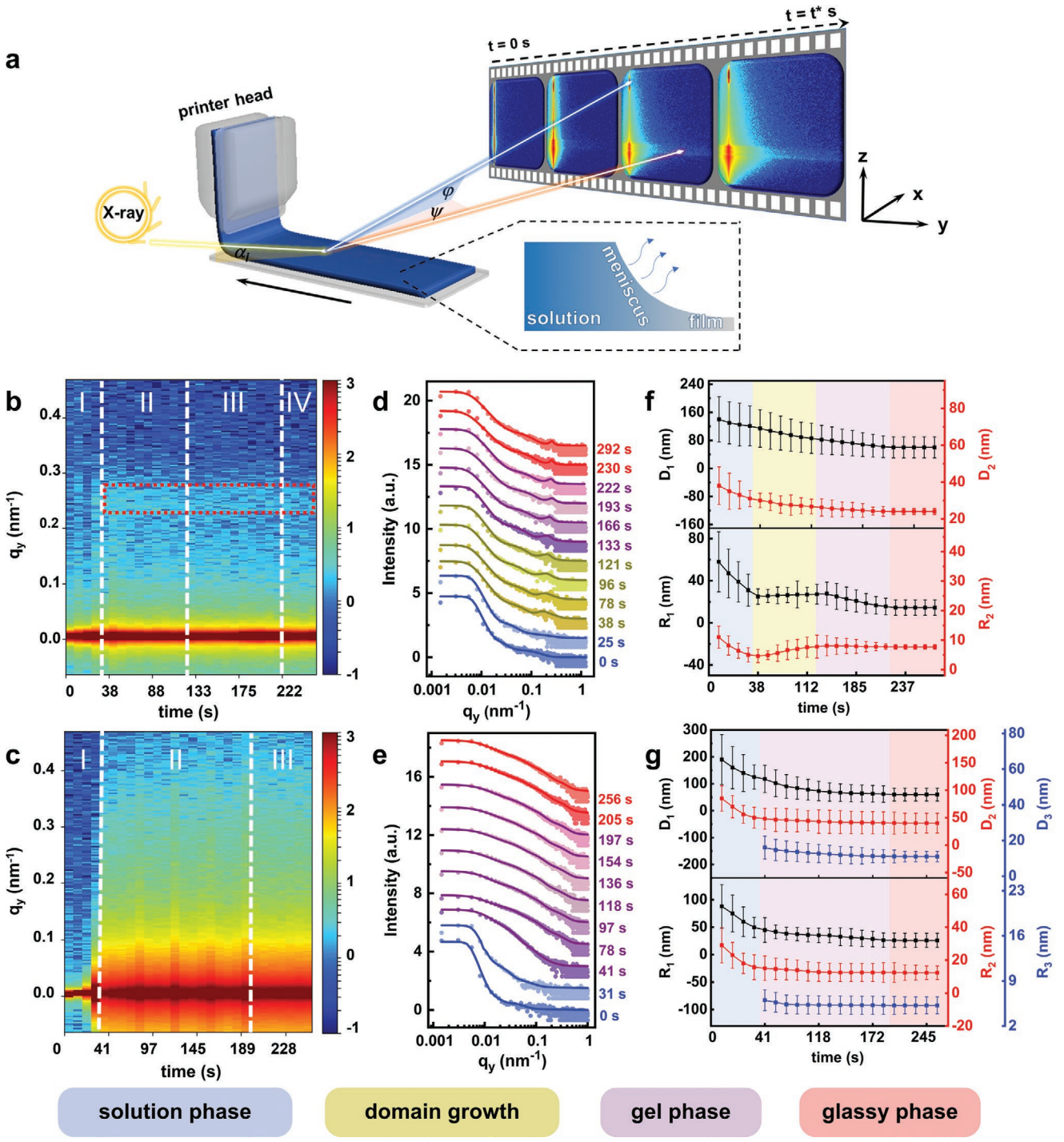

Figure 3. a) Schematic of the in situ slot-die coating setup. Temporal evolution of the inner structures for the slot-die-coated b,d,f) PS-*b*-PEO film and c,e,g) PS-*b*-PEO/ZnO hybrid film. b,c) 2D color mappings of horizontal line cuts extracted from the 2D GISAXS data plotted as a function of time. All horizontal line cuts are integrated over the corresponding Yoneda region. Four stages (I–IV) are seen for PS-*b*-PEO and three stages (I–III) for PS-*b*-PEO/ZnO film formation as indicated with vertical dashed lines. The red dashed rectangle in (b) highlights the appearance and the evolution of the Bragg peak originating from the PEO domain spacing. d,e) Representative horizontal line cuts (hollow circles) together with corresponding modeling fits (solid lines) plotted from the bottom (wet film) to top (glassy film) with increasing time. For clarification, all data are shifted along the *y*-axis. f,g) Characteristic structure parameters extracted from the fits are the interdomain distances (*D*) and the domain radius (*R*). Blue, yellow, violet, and red shading denote the stages involved in structure evolution as indicated.

the scattering peak appears at 38 s. Reflected by the FWHM of the scattering peak (Figure S11, Supporting Information), the order continues to improve until 222 s, which can be attributed to stronger segmental interactions arising from the increased

Flory–Huggins interaction parameters (χ) due to solvent loss. During the whole film formation process, two sets of structures are sufficient for the GISAXS line cut modeling and the determined parameters are summarized in Figure 3f. These results categorize the film formation process for PS-*b*-PEO film into four stages. Despite the lateral distance between the adjacent PEO domains showing a progressively decreasing tendency before reaching the final stable status, the most significant decrease is found to be within the first 25 s, which can be denoted as the solution phase (stage I). Concomitantly, the PEO domains also feature a rapid shrinkage with the large-sized object radius, R_1, drastically decreasing from 58 ± 23 to 31 ± 12 nm and the small-sized object radius R_2 decreasing from 11 ± 3 to 5.0 ± 1.0 nm. Furthermore, the size of the PS domain (R_{PS}) can be calculated based on the following equation[63]

$$2\times\text{PS domain radius} = \text{PEO interdomain distance} - (2\times\text{PEO domain radius}) \quad (1)$$

Therefore, the onset values for small-sized PS domains and large-sized PS domains are estimated to be around 9 and 15 nm, respectively. The former one matches perfectly the radius of the PS core obtained from the SAXS analysis, while the latter one might be associated with the compound micelles formed by an abrupt solvent loss upon hitting the hot substrate. From this point of view, the scattering intensity collected in stage I is mainly contributed by the micelles. At the end of this stage, the small-sized and large-sized PS domains increase to 12.3 and 29.5 nm, respectively. Strikingly, the shrinkage of the PEO shell occurs with the concomitant expansion of the PS core, which would result in an improved degree of stretching of the core and lead to a continuous loss of the entropy. Consequently, a morphology change toward lower curvature cylindrical structures occurs to resolve the interfacial instability it generates.[60] Considering a non-negligible spatial correlation as described by the hard-sphere structure factor in SAXS analysis, the coalescence between spherical micelles would also be facilitated by further narrowing the interdistance. According to the solvent evaporation-induced self-assembly mechanism, the directional solvent gradient along the substrate normal could enable the formation of ordered PS-*b*-PEO nanostructures.[64] Calculated by the well-pronounced scattering peak at $q \approx 0.20$ nm^{-1}, a periodic interdomain distance of 31 nm of PEO cylinders is seen, initializing the domain growth (stage II). Simultaneously, a slow enlargement of the PEO domain radius (R_1: [25 ± 5] – [28 ± 8] nm, R_2: [4.6 ± 1.0] – [8 ± 3] nm) is found, which is typical of a morphology coarsening. From the physical point of view, the coupling of Lifshitz–Slyozov–Wagner (or Ostwald ripening) mechanism and Sigga's mechanism could be responsible for the growth of the domain size considering the intermediate PEO volume fraction. The former one is characteristic of the evaporation from smaller droplets and then condensation into nearby larger droplets, which is mainly driven by the translational diffusion of the constituent materials. While the latter is a hydrodynamic process driven by the interfacial tension between PS and PEO phases.[65] However, the growth of the PEO domain does not proceed infinitely and once it comes to a critical point, the system would begin to dehydrate and transit into stage III. Indeed, both stage II and stage III can be regarded as gel phases in terms of the solvent contents in these wet films during drying. Featuring a smooth decrease of the PEO sizes (R_1: [25 ± 10] – [16 ± 7] nm, R_2: [8 ± 2] – [7.8 ± 1.0] nm), this stage indicates that the solvent loss outcompetes the morphology coarsening and dominates the dimension changes. At the end of stage III, the length scales for both, domain radius and interdomain distance reach their minimum and maintain constants in stage IV, which is in perfect accordance with the values retrieved from the corresponding ex situ GISAXS results. Taking the vitrification of the PS phase into account, the formed nanostructures are solidified and preserved as the majority of solvent molecules is removed. Thus, the polymer film throughout the course of stage IV is in its glassy state.

2.3.2. Slot-Die Coating of Polystyrene-block-Poly(Ethylene Oxide)/ZnO Hybrid Film

Likewise, the structure evolution of the hybrid film is also followed with the analysis of in situ GISAXS data. The horizontal line cuts of the 2D GISAXS data are performed at the critical angle of PEO/ZnO and plotted as a mapping in Figure 3c. Selected 2D GISAXS data are found in Figure S10, Supporting Information. Due to the loading of phase-selective ZnO, the PS-*b*-PEO/ZnO hybrid film follows a different scattering behavior. It has a stronger scattering contrast and lacks characteristic scattering peaks throughout the whole film formation process. Immediately at the beginning of the printing process, again a low scattering intensity is observed due to the diluted ink being deposited. As the concentration of the PS-*b*-PEO/ZnO hybrid starts to rise via solvent evaporation, the scattering intensity is enhanced. It is followed by a longer period with a less pronounced intensity increase before an equilibrium is reached. The small intensity fluctuations observed in the 2D mappings for both slot-die coatings can be understood as slight film inhomogeneities and fluctuations produced by local solution evaporation along the printing direction in the meniscus-guided solution casting techniques.[66] The time-resolved horizontal line cuts are shown together with the fits in Figure 3e. A steep intensity decay in the intermediate q_y range is prominent during the initial 31 s, being characteristic of a limited scattering contribution from the well-dissolved solutes. As solvent evaporation progresses, this scattering feature vanishes. Instead, a shoulder emerges and slightly shifts toward higher q_y values and then remains unaltered during the subsequent time, which is closely associated with the formation and the development of the smallest structures. Similarly, by fitting the in situ horizontal line cuts in a quantitative manner, the time-dependent structure evolution is determined (Figure 3g). Only three stages are identified from structure changes. Two sets of structures can successfully model the scattering data in stage I, while an additional set of structures is mandatory for the later stages II and III. Similar to the pure DBC film, we observe a successively decreasing tendency for the separation distance. Without involving any phase ripening process observed in the pure DBC film, the domain size of the hybrid film, however, is a monotonous function of time until decreasing to the final values. More specifically, a drastic reduction of the PEO/ZnO domain size

(R_1: [88 ± 36] – [49 ± 14] nm, R_2: [29 ± 8] – [15 ± 4] nm) for two structures is again found in stage I, which can be attributed to the fast solvent evaporation in the solution phase. Along with the emergence of the third set of structures, stage II undergoes a reduced decrease for all structural parameters (R_1: [44 ± 21] – [26 ± 12] nm, R_2: [15 ± 7] – [12 ± 4] nm, R_3: [6.0 ± 1.0] – [5.0 ± 1.0] nm) until reaching the minimum at t = 197 s, and then changes into stage III, which describes the final film. Notice that no domain growth process can be observed throughout the complete film formation process for the hybrid film. Instead, due to the integration of ZnO, the hybrid film has a larger Flory–Huggins interaction parameter, which suggests that the PEO/ZnO domains have relatively stronger incompatibility against PS domains and are more prone to lead to multilength phase separation during the solvent loss in stage II.[67]

As confirmed from the ex situ GISAXS results of the PS-*b*-PEO/ZnO hybrid film, the parameters extracted in stage III are indicative of a completely solidified film. In contrast to the pure DBC film, stage II encountered here denotes the gel phase and stage III the glassy phase. The hydrogen bonding between PEO segments and ZnO nanoparticles is commonly believed to largely suppress the further motions of PEO chains. Therefore, the hybrid film printing can be regarded as a more easily controllable printing process than the pure DBC film printing because fewer stages are involved in the film formation process. As seen in the trimodal domain size distribution in the gel phase, the highest intensities observed for the peak centered at the smallest size at 41 s indicate the largest amount of the smallest PEO/ZnO domains inside the hybrid film (Figure S12, Supporting Information). Moreover, the increasing peak intensity of the smallest PEO/ZnO domains in the following drying process is accompanied by the decrease from the middle-sized and large-sized ones. Therefore, it is reasonable to conclude that the emergence and enrichment of small PEO/ZnO domains happen at the sacrifice of the larger domains. Extracted from the peak intensities, the number fraction of the smallest domains reaches 88% at the end of the gel phase. Based on the cylindrical shape for all scattering objects, the volume fractions of the smallest PEO/ZnO domains can be estimated to be 45%, correspondingly.

2.3.3. Morphology Transformation Pathways during Slot-Die Coating

For both, the PS-*b*-PEO and PS-*b*-PEO/ZnO hybrid film,[62] the abovementioned in situ and ex situ studies probe the structural developments during slot-die coating. In conjunction with the micelle information, they provide crucial clues for a better understanding of the morphology transformation pathways during the solution-to-film transition. In the initial solution stage, the PS blocks can be regarded as the guest phase hosted by the PEO + solvents (for PS-*b*-PEO) or PEO + ZnO + solvents (for PS-*b*-PEO/ZnO) environment due to the solvent selectivity. In the final solidified films, however, the PS blocks constitute the matrix to host the minor PEO or PEO/ZnO phase. It is probably that in the film formation process the solvent evaporation is responsible for the inversion of the guest–host roles. Notwithstanding that H_2O will leave the film first at a much faster evaporation rate due to its lower boiling point and higher vapor pressure, precise tracking of solvent content is intrinsically limited by the used GISAXS geometry. In addition, the volume of DMF in the binary solvent mixtures is far higher than that of water (V_{DMF}:V_{H2O} = 181). Therefore, the effect of H_2O during the film formation process can be negligible herein. Regarding the difference in morphology evolution, the ZnO–PEO interaction plays a crucial role in the competition between the crystallization behavior of the PEO block and the phase separation between PS and PEO (PS and PEO/ZnO for the hybrid film).

The observed respective film formation process is depicted in **Figure 4**c,d. Beginning with the solution phase, the initial shape difference can be explained by the mediated interfacial energy due to the hydrogen bonding between ZnO and PEO. Regardless of the presence of ZnO, the interplay between high chain mobilization and high segmental interactions dictates the film formation process for both cases to a large extent. Such a short timescale observed in stage I is originating from the presence of abundant solvent molecules in the solution phase, which enables a high diffusive displacement rate for polymer chains and thereby allows for a fast assembly. As the viscosity increases when the concentration of solutes rises with continuous solvents loss, the films develop into the gel phase with a slower structure formation rate. Subsequently, the films are completely solidified by the glass transition of the PS phase. Strikingly, the most significant changes encountered in stage I for both cases trigger the structural transition in stage II, where a new structure emerges, laying the foundation of architectures that determine the ultimate phase-separated film morphologies. In the case of the pure DBC, the driving force for the configuration change from core–shell sphere to short-range ordered cylinders is associated with the proceeding reduction of the volume fraction between the PEO shell and the PS core.[60] In another respect, it appears that the solvent evaporation would promote the coalescence of micelles due to the narrowing of intermicellar distances.[68] Starting at the formation of cylinders, the pre-existing domains start to grow. According to ex situ GIWAXS results, there must be a crystallization process involved during the self-assembly. Therefore, a plausible reason is that the crystallization process dominates stage II and the relevant crystal growth of PEO provokes the domain growth.[67] As the films turn into a more solid-rich state, the PEO domains in the pure DBC film terminate the growth and switch to shrinkage at stage III, where the rate of structure evolution is rather slow and further organization toward a more ordered phase-separated state is hindered due to greater limitations from solvent diffusion. Although the PEO crystallization process may continue beyond the time scale of stage II and proceed marginally through stage III, the film in stage III is dominated by its drying behavior, indicating that the system is strongly limited by the deceleration of the chain motion.

The Flory–Huggins interaction parameter (χ) between ZnO and PEO is negative due to the hydrogen bonding, which would favor the mixing of them in the co-assembly process of the hybrid film. Thus, squeezing out of ZnO from the PEO domains is not possible. However, there is also an energetically unfavorable conformation loss arising from the PEO chains

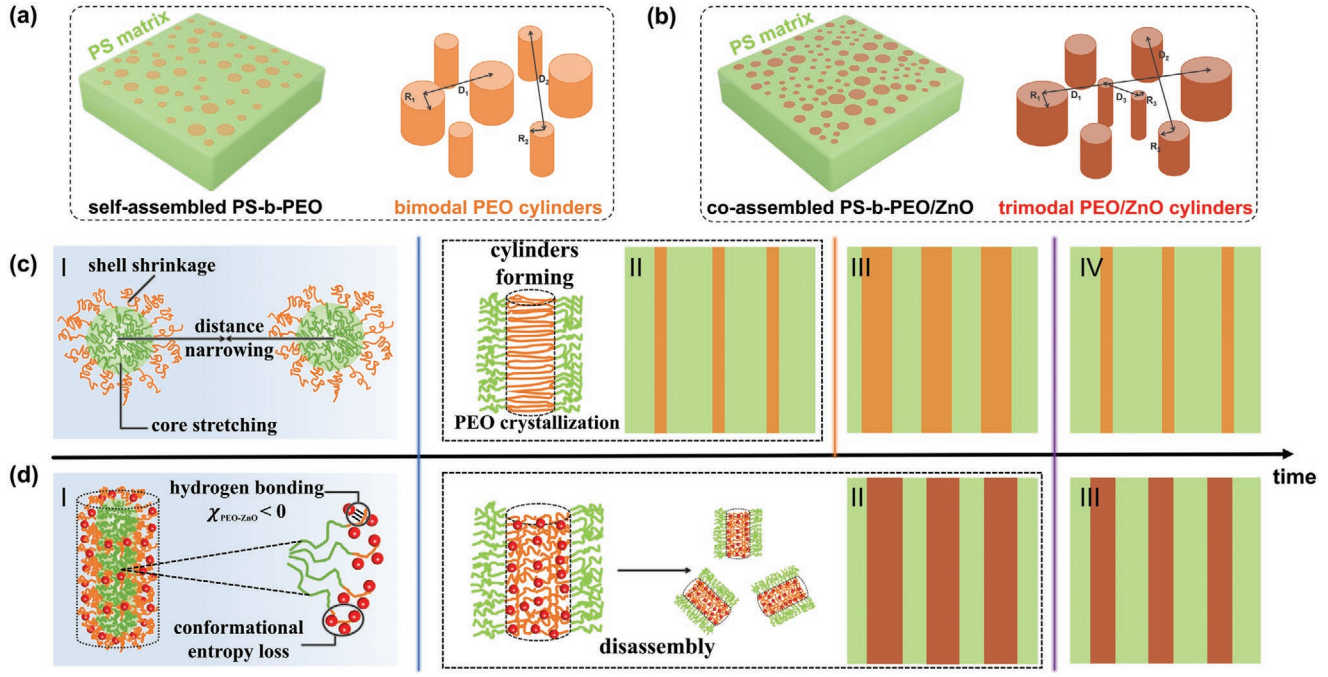

Figure 4. Final morphologies of a) neat PS-*b*-PEO films and b) PS-*b*-PEO/ZnO hybrid films as modeled with GISAXS. Sketch of proposed pathways for the structural evolution during slot-die coating. Schematic illustrations of c) neat PS-*b*-PEO films and d) PS-*b*-PEO/ZnO hybrid films. The stages I, II, III and IV in (c) represent the solution phase, domain growth, gel and glassy phase, respectively, while the stages I, II and III in (d) denote the solution, gel and glassy phase, respectively.

tethering to the ZnO nanoparticles, which is attributed to be the main reason for the generation of the third set of structures. As the solvent content decreases, the increased phase separation propensity places strong limitations on the conformations that the PEO chains are able to take. At a critical point when the stretching degree of the PEO chains is drastically reduced and complete accommodation of ZnO is greatly constrained, the disassembly into smaller structures would take place.[69,70] As mentioned above, no crystallization behavior can be observed for the PS-*b*-PEO/ZnO hybrid film, implying that the disassembly manipulates the phase separation in the entire gel phase period.

As one of the key factors, the wetting behavior has been reported to affect the morphology evolution via altering the interaction between the substrate surface and the film.[71] As presented in Figure S13, Supporting Information, the drop contact angles of both, pure polymer and hybrid solutions show no substantial difference, which is indicative of a negligible effect of ZnO incorporation on the wetting behavior. Note that DMF has a high boiling point and low vapor pressure. Thus, it is inevitable that part of solvent residuals could remain inside the films and it can only be completely expelled by additional thermal annealing. Therefore, both films at the ultimate stage are defined as solidified rather than dry due to the vitrification of the PS phase. For the pure DBC, stage I (25 s) occurs through a fast solvent evaporation in a much shorter timescale than the subsequent micellar growth and drying process in the gel phase (stage II + stage III: 184 s). It is interesting to note that the solution phase (stage I: 31 s) and gel phase (stage III: 156 s) in the hybrid film is comparable to that, suggesting that the complete establishment of a solidified film is only slightly dependent on the material constitutes. More significantly, the extended timescale stemming from the slow solvent evaporation seems to be responsible for achieving well-organized structures immediately after film formation.

3. Conclusion

In summary, the film formation process during slot-die coating is complex. Both co-assembly and self-assembly pathways during the solution-to-film transition are involving multistep structural transformations triggered by solvent evaporation. Benefiting from the extended time window in slot-die coating technique as compared with fast casting methods such as spin coating, both systems (bare DBC and hybrid) have sufficient chain mobility for further structural reorganization, thereby approaching equilibrium structures. Both final films exhibit similar cylindrical morphologies, however, the preferential segregation of ZnO inside the PEO blocks causes the domain expansion of PEO itself and more importantly, the solidification kinetics they follow are inherently different. As for the establishment of the neat PS-*b*-PEO film, the determining step is the formation of a cylindrical phase from spherical micelles triggered by the shell shrinkage and core expansion caused by fast solvent evaporation. Indeed, the high chain mobility during this solvent-rich stage enables the fast coalescence of the spherical micelles and subsequent development into ordered cylindrical domains. Whereas for PS-*b*-PEO/ZnO solution, the morphology of the hybrid micelles is not faithfully derived from spherical PS-*b*-PEO micelles. Intriguingly, the incorporation of the ZnO precursor facilitates directional fusions of spherical PS-*b*-PEO micelles toward cylindrical PS-*b*-PEO/ZnO aggregates. As in this hybrid system, the occurrence of multi-length scale structures during the subsequent drying periods

is pivotal that allows further development toward final well-separated structures. Moreover, the intermolecular interactions between PEO and ZnO via hydrogen bonding frustrates the PEO crystallization, thereby leading to the absence of domain growth throughout the film formation process for the hybrid film.

By comparing the phase separation behaviors of the pure DBC and the hybrid system from the solution to solid film states, we follow the self-assembly of pure DBCs and co-assembly of DBCs-directed hybrid structures. Understanding of such an interplay between the DBCs acting as nano-templates and the guest phase molecules enables a particularly precise control of the synthesis conditions to achieve the desirable morphologies. The fine tailoring of solidification kinetics through solvent affinity and evaporation rates, precursor categories and concentration, and deposition methods and parameters, constitutes a multifaceted platform for obtaining periodically equilibrium nanophases as predicted by the theoretical phase diagram. In addition, in situ GISAXS, an ideal real-time characterization technique, can investigate the impacts of these factors on the morphology evolution and provide in-depth insights into the fundamental mechanisms. These findings herein can be applicable to other DBCs systems or hybrid films synthesis in a block copolymer assisted sol–gel route and can promote further morphology optimization to produce highly ordered functional nanomaterials with reliable control.

Supporting Information

Supporting Information is available from the Wiley Online Library or from the author.

Acknowledgements

This work was supported by funding from the Deutsche Forschungsgemeinschaft (DFG, German Research Foundation) under Germany's Excellence Strategy – EXC 2089/1 – 390776260 (e-conversion) and the International Research Training Group 2022 Alberta/Technical University of Munich International Graduate School for Environmentally Responsible Functional Hybrid Materials (ATUMS), TUM.solar in the context of the Bavarian Collaborative Research Project Solar Technologies Go Hybrid (SolTech), and the Center for NanoScience (CeNS). T.T., S.Y., S.T., and S.L. acknowledge the financial support from China Scholarship Council (CSC) and K.S.W. from the Hans Böckler Stiftung. The authors thank Prof. Alexander Holleitner and Peter Weiser for providing access to the SEM, Yanan Li for help with the SAXS measurements, Jia-Jhen Kang with SAXS data analysis, and Florian A. Jung with the DLS measurements. All GISAXS measurements were carried out at the light source PETRA III at DESY, a member of the Helmholtz Association (HGF).

Open access funding enabled and organized by Projekt DEAL.

Conflict of Interest

The authors declare no conflict of interest.

Data Availability Statement

Data available on request from the authors.

Keywords

film formation, in situ grazing-incidence small-angle X-ray scattering, printing, slot-die coatings, ZnO hybrids

Received: June 11, 2021
Revised: July 14, 2021
Published online: August 12, 2021

[1] Z. L. Wang, *Mater. Today* **2004**, *7*, 26.
[2] L. Schmidt-Mende, J. L. MacManus-Driscoll, *Mater. Today* **2007**, *10*, 40.
[3] M. Y. Guo, A. M. C. Ng, F. Liu, A. B. Djurišić, W. K. Chan, H. Su, K. S. Wong, *J. Phys. Chem. C* **2011**, *115*, 11095.
[4] H. Zeng, W. Cai, P. Liu, X. Xu, H. Zhou, C. Klingshirn, H. Kalt, *ACS Nano* **2008**, *2*, 1661.
[5] J. Wang, X. Li, Y. Xia, S. Komarneni, H. Chen, J. Xu, L. Xiang, D. Xie, *ACS Appl. Mater. Interfaces* **2016**, *8*, 8600.
[6] A. Menzel, K. Subannajui, F. Güder, D. Moser, O. Paul, M. Zacharias, *Adv. Funct. Mater.* **2011**, *21*, 4342.
[7] G. Wang, J. Qin, X. Zhou, Y. Deng, H. Wang, Y. Zhao, J. Wei, *Adv. Funct. Mater.* **2018**, *28*, 1806144.
[8] J. Zhou, N. S. Xu, Z. L. Wang, *Adv. Mater.* **2006**, *18*, 2432.
[9] H. M. Xiong, *Adv. Mater.* **2013**, *25*, 5329.
[10] M. Law, L. E. Greene, J. C. Johnson, R. Saykally, P. Yang, *Nat. Mater.* **2005**, *4*, 455.
[11] Q. Zhang, C. S. Dandeneau, X. Zhou, G. Cao, *Adv. Mater.* **2009**, *21*, 4087.
[12] Y. Mai, A. Eisenberg, *Chem. Soc. Rev.* **2012**, *41*, 5969.
[13] E. Kim, Y. Vaynzof, A. Sepe, S. Guldin, M. Scherer, P. Cunha, S. V. Roth, U. Steiner, *Adv. Funct. Mater.* **2014**, *24*, 863.
[14] C. Li, Q. Li, Y. V. Kaneti, D. Hou, Y. Yamauchi, Y. Mai, *Chem. Soc. Rev.* **2020**, *49*, 4681.
[15] M. C. Orilall, U. Wiesner, *Chem. Soc. Rev.* **2011**, *40*, 520.
[16] W. Li, Q. Yue, Y. Deng, D. Zhao, *Adv. Mater.* **2013**, *25*, 5129.
[17] X. Zhou, Y. Zou, J. Ma, X. Cheng, Y. Li, Y. Deng, D. Zhao, *Chem. Mater.* **2019**, *31*, 8112.
[18] K. Sarkar, M. Rawolle, E. M. Herzig, W. Wang, A. Buffet, S. V. Roth, P. Müller-Buschbaum, *ChemSusChem* **2013**, *6*, 1414.
[19] Y. J. Cheng, J. S. Gutmann, *J. Am. Chem. Soc.* **2006**, *128*, 4658.
[20] K. Wang, S. Xia, W. Cao, N. Hohn, S. Grott, L. P. Kreuzer, M. Schwartzkopf, S. V. Roth, P. Müller-Buschbaum, *ACS Appl. Nano Mater.* **2018**, *1*, 7139.
[21] D. Gu, F. Schuth, *Chem. Soc. Rev.* **2014**, *43*, 313.
[22] K. Wang, V. Körstgens, D. Yang, N. Hohn, S. V. Roth, P. Müller-Buschbaum, *J. Mater. Chem. A* **2018**, *6*, 4405.
[23] K. Sarkar, C. J. Schaffer, D. M. González, A. Naumann, J. Perlich, P. Müller-Buschbaum, *J. Mater. Chem. A* **2014**, *2*, 6945.
[24] A. Sandstrom, H. F. Dam, F. C. Krebs, L. Edman, *Nat. Commun.* **2012**, *3*, 1002.
[25] C. M. Palumbiny, F. Liu, T. P. Russell, A. Hexemer, C. Wang, P. Müller-Buschbaum, *Adv. Mater.* **2015**, *27*, 3391.
[26] H. Zhao, H. B. Naveed, B. Lin, X. Zhou, J. Yuan, K. Zhou, H. Wu, R. Guo, M. A. Scheel, A. Chumakov, *Adv. Mater.* **2020**, *32*, 2002302.
[27] F. C. Krebs, *Sol. Energy Mater. Sol. Cells* **2009**, *93*, 394.
[28] X. Gu, L. Shaw, K. Gu, M. F. Toney, Z. Bao, *Nat. Commun.* **2018**, *9*, 1.
[29] P. Müller-Buschbaum, *Adv. Mater.* **2014**, *26*, 7692.
[30] F. Liu, S. Ferdous, E. Schaible, A. Hexemer, M. Church, X. Ding, C. Wang, T. P. Russell, *Adv. Mater.* **2015**, *27*, 886.
[31] S. Pröller, F. Liu, C. Zhu, C. Wang, T. P. Russell, A. Hexemer, P. Müller-Buschbaum, E. M. Herzig, *Adv. Energy Mater.* **2016**, *6*, 1501580.

[32] X. Gu, I. Gunkel, A. Hexemer, W. Gu, T. P. Russell, *Adv. Mater.* **2014**, *26*, 273.
[33] A. V. Berezkin, F. Jung, D. Posselt, D. M. Smilgies, C. M. Papadakis, *Adv. Funct. Mater.* **2018**, *28*, 1706226.
[34] L. Song, W. Wang, V. Körstgens, D. M. González, F. C. Löhrer, C. J. Schaffer, J. Schlipf, K. Peters, T. Bein, D. Fattakhova-Rohlfing, S. V. Roth, P. Müller-Buschbaum, *Nano Energy* **2017**, *40*, 317.
[35] K. Sarkar, E. V. Braden, S. Pogorzalek, S. Yu, S. V. Roth, P. Muller-Buschbaum, *ChemSusChem* **2014**, *7*, 2140.
[36] G. Fleury, D. Hermida-Merino, D. Jingjin, K. Aissou, A. Bytchkov, G. Portale, *Adv. Funct. Mater.* **2019**, *29*, 1806741.
[37] J. J. van Franeker, D. Hermida-Merino, C. Gommes, K. Arapov, J. J. Michels, R. A. Janssen, G. Portale, *Adv. Funct. Mater.* **2017**, *27*, 1702516.
[38] T. Hu, F. Li, K. Yuan, Y. Chen, *ACS Appl. Mater. Interfaces* **2013**, *5*, 5763.
[39] P. Fan, D. Zhang, Y. Wu, J. Yu, T. P. Russell, *Adv. Funct. Mater.* **2020**, *30*, 2002932.
[40] L. Zhu, S. Cheng, B. Calhoun, Q. Ge, R. Quirk, E. Thomas, B. Hsiao, F. Yeh, B. Lotz, *Polymer* **2001**, *42*, 5829.
[41] L. Paseta, G. Potier, S. Abbott, J. Coronas, *Org. Biomol. Chem.* **2015**, *13*, 1724.
[42] B. J. Ree, J. Lee, Y. Satoh, K. Kwon, T. Isono, T. Satoh, M. Ree, *Polymers* **2018**, *10*, 1347.
[43] Y.-J. Cheng, S. Zhou, M. Wolkenhauer, G.-G. Bumbu, S. Lenz, M. Memesa, S. Nett, S. Emmerling, W. Steffen, S. V. Roth, J. S. Gutmann, *Eur. J. Inorg. Chem.* **2014**, *2014*, 836.
[44] S.-W. Yeh, K.-H. Wei, Y.-S. Sun, U.-S. Jeng, K. S. Liang, *Macromolecules* **2003**, *36*, 7903.
[45] D. Lombardo, G. Munao, P. Calandra, L. Pasqua, M. T. Caccamo, *Phys. Chem. Chem. Phys.* **2019**, *21*, 11983.
[46] U.-S. Jeng, Y.-S. Sun, H.-Y. Lee, C.-H. Hsu, K. S. Liang, S.-W. Yeh, K.-H. Wei, *Macromolecules* **2004**, *37*, 4617.
[47] R. S. Hafez, N. A. Hakeem, A. A. Ward, A. M. Ismail, F. H. A. El-kader, *J. Inorg. Organomet. Polym. Mater.* **2020**, *30*, 4468.
[48] D. Kiefer, L. Yu, E. Fransson, A. Gomez, D. Primetzhofer, A. Amassian, M. Campoy-Quiles, C. Muller, *Adv. Sci.* **2017**, *4*, 1600203.
[49] Y.-W. Chen, B.-J. Yeh, T. Hashimoto, S.-Y. Liao, C.-T. Lo, *Macromolecules* **2018**, *51*, 7699.
[50] C.-H. Ko, C. Henschel, G. P. Meledam, M. A. Schroer, P. Müller-Buschbaum, A. Laschewsky, C. M. Papadakis, *Macromolecules* **2020**, *54*, 384.
[51] J.-J. Kang, F. A. Jung, C.-H. Ko, K. Shehu, L. C. Barnsley, F. Kohler, H. Dietz, J. Zhao, S. Pispas, C. M. Papadakis, *Macromolecules* **2020**, *53*, 4068.
[52] T. Rejek, P. Schweizer, D. Joch, L. Portilla, E. Spiecker, M. Halik, *Macromolecules* **2020**, *53*, 5604.
[53] A. E. Di Mauro, M. Striccoli, N. Depalo, E. Fanizza, L. Cano, C. Ingrosso, A. Agostiano, M. L. Curri, A. Tercjak, *Soft Matter* **2014**, *10*, 1676.
[54] D. W. Weller, L. Galuska, W. Wang, D. Ehlenburg, K. Hong, X. Gu, *Macromolecules* **2019**, *52*, 5026.
[55] X. Ding, J. Liu, T. A. L. Harris, *AIChE J.* **2016**, *62*, 2508.
[56] Y. Yao, E. Metwalli, B. Su, V. Korstgens, D. M. Gonzalez, A. Miasnikova, A. Laschewsky, M. Opel, G. Santoro, S. V. Roth, P. Muller-Buschbaum, *ACS Appl. Mater. Interfaces* **2015**, *7*, 13080.
[57] A. E. Di Mauro, M. Striccoli, N. Depalo, E. Fanizza, L. Cano, C. Ingrosso, A. Agostiano, M. L. Curri, A. Tercjak, *Soft Matter* **2014**, *10*, 1676.
[58] S. Roth, M. Kuhlmann, H. Walter, A. Snigirev, I. Snigireva, B. Lengeler, C. Schroer, M. Burghammer, C. Riekel, P. Müller-Buschbaum, *J. Phys.: Condens. Matter* **2009**, *21*, 264012.
[59] M. Schwartzkopf, S.-J. Wöhnert, V. Waclawek, N. Carstens, A. Rothkirch, J. Rubeck, M. Gensch, J. Drewes, O. Polonskyi, T. Strunskus, A. M. Hinz, S. J. Schaper, V. Körstgens, P. Müller-Buschbaum, F. Faupel, S. V. Roth, *Nanoscale Horiz.* **2020**, *6*, 132.
[60] K. Yu, A. Eisenberg, *Macromolecules* **1996**, *29*, 6359.
[61] S. Xia, E. Metwalli, M. Opel, P. A. Staniec, E. M. Herzig, P. Müller-Buschbaum, *ACS Appl. Mater. Interfaces* **2018**, *10*, 2982.
[62] C. X. Cheng, Y. Tian, Y. Q. Shi, R. P. Tang, F. Xi, *Langmuir* **2005**, *21*, 6576.
[63] L. Song, A. Abdelsamie, C. J. Schaffer, V. Körstgens, W. Wang, T. Wang, E. D. Indari, T. Fröschl, N. Hüsing, T. Haeberle, P. Lugli, S. Bernstorff, P. Müller-Buschbaum, *Adv. Funct. Mater.* **2016**, *26*, 7084.
[64] S. H. Kim, M. J. Misner, T. Xu, M. Kimura, T. P. Russell, *Adv. Mater.* **2004**, *16*, 226.
[65] R. Shimizu, H. Tanaka, *Nat. Commun.* **2015**, *6*, 7407.
[66] J. B. Whitaker, D. H. Kim, B. W. Larson, F. Zhang, J. J. Berry, M. F. A. M. van Hest, K. Zhu, *Sustainable Energy Fuels* **2018**, *2*, 2442.
[67] Z. Wang, K. Gao, Y. Kan, M. Zhang, C. Qiu, L. Zhu, Z. Zhao, X. Peng, W. Feng, Z. Qian, X. Gu, A. K. Jen, B. Z. Tang, Y. Cao, Y. Zhang, F. Liu, *Nat. Commun.* **2021**, *12*, 332.
[68] Y. Ren, Y. Zou, Y. Liu, X. Zhou, J. Ma, D. Zhao, G. Wei, Y. Ai, S. Xi, Y. Deng, *Nat. Mater.* **2020**, *19*, 203.
[69] Z. Hua, J. R. Jones, M. Thomas, M. C. Arno, A. Souslov, T. R. Wilks, R. K. O'Reilly, *Nat. Commun.* **2019**, *10*, 5406.
[70] S. C. Warren, F. J. Disalvo, U. Wiesner, *Nat. Mater.* **2007**, *6*, 156.
[71] S. C. Park, B. J. Kim, C. J. Hawker, E. J. Kramer, J. Bang, J. S. Ha, *Macromolecules* **2007**, *40*, 8119.